

Additively manufactured CrMnFeCoNi/AlCoCrFeNiTi_{0.5} laminated high-entropy alloy with enhanced strength-plasticity synergy

S. Guan ^a, D. Wan ^b, K. Solberg ^b, F. Berto ^b, T. Welo ^b, T.M. Yue ^a, K.C. Chan ^{a,*}

^a Advanced Manufacturing Technology Research Center, Department of Industrial and Systems Engineering, The Hong Kong Polytechnic University, Hung Hom, Kowloon, Hong Kong

^b Department of Mechanical and Industrial Engineering, Norwegian University of Science and Technology, Richard Birkelands vei 2B, 7491 Trondheim, Norway

* Corresponding author.

Email address: kc.chan@polyu.edu.hk (K.C. Chan)

Abstract

In this study, we additively manufactured a CrMnFeCoNi/AlCoCrFeNiTi_{0.5} laminated high-entropy alloy (HEA), with alternating layers of both constituent materials, that exhibits enhanced strength-plasticity synergy during compression (yield strength up to 990 MPa and no complete fracture until 80% strain), surpassing those of monolithic bulk HEAs. The enhanced strength-plasticity synergy originates from heterogenous microstructures of ultra-hard body-centered-cubic equiaxed grains and soft face-centered-cubic columnar grains periodically arranged in the AlCoCrFeNiTi_{0.5} and CrMnFeCoNi lamellae respectively. This study demonstrates a feasible and flexible way to design HEAs with heterogenous microstructures and superior mechanical properties.

Keywords: Additive manufacturing; Laminated high-entropy alloy; Heterogenous microstructure; Strength-plasticity synergy

Deviating from conventional alloys with a single major element, high-entropy alloys (HEAs) comprise multiple principal elements, often 5 or more, with each between 5 and 35 at.% [1]. Such a new and near-infinite compositional space provides near-infinite possibilities, and some HEAs have been reported to exhibit exceptional properties (e.g. cryogenic fracture-toughness [2]) and show promising applications, which have aroused considerable amount of interest in the field of metallic materials. However, similar to most conventional alloys, HEAs often show a paradox of strength and plasticity. More specifically, face-centered-cubic (FCC) HEAs (e.g. CrMnFeCoNi) are ductile, but typically not strong [2, 3]. In contrast, body-centered-cubic (BCC) HEAs (e.g. AlCoCrFeNiTi_{0.5}) are strong, but usually sacrifice plasticity [4-6]. Although a few HEAs with multi-phase (e.g. FCC + BCC) microstructures and balanced mechanical properties have recently been designed [7, 8], composition design is a trial-and-error routine. Furthermore, it is worth mentioning that the vast majority of HEAs were processed by casting, possibly followed by cold deformation and subsequent annealing [9]. Nearly all these conventional approaches require post machining which is not applicable to the complex geometry parts for practical applications.

In pursuit of the enhancement in the strength-plasticity synergy of HEAs, we were inspired by laminated conventional alloys that integrate multi-materials and hence multi-phases with distinct properties [10]. Heterogeneities in compositions, phases and microstructures can often result in properties enhancement, as can be seen from laminated steels [10], compositionally graded steels [10-12], etc. It has been demonstrated that several micro-mechanisms, e.g. crack bridging [13] and crack blunting [14], can be induced by the laminated microstructures. By introducing this

approach, we believe that laminated HEAs with distinct phases and microstructures can circumvent the dilemma of the strength-plasticity trade-off of monolithic HEAs. Conventional lamination routes include diffusion bonding [15], reaction bonding [13, 16, 17], deformation bonding [18-22], etc. Whereas, in the present study, we adopted the laser powder-blown additive manufacturing (AM) process, rather than those conventional routes, to synthesize the laminated HEAs (i.e. CrMnFeCoNi/AlCoCrFeNiTi_{0.5}). The laser powder-blown AM process allows the simultaneous manufacturing of laminated structures and complex-shaped parts via alternate deposition of multiple powdered materials layer-upon-layer, with little or no post machining required. Furthermore, the AM process is characterized by highly localized (i.e. localized into melt pools) melting and solidification processes, and hence generates unique microstructures that are not easily accessible via conventional metallurgical routes [23]. To the best of our knowledge, this work is the first attempt to achieve laminated HEAs by the laser powder-blown AM process and to understand the microstructures and mechanical behavior, although there have been a few successful attempts to synthesize monolithic HEAs by the AM process in the recent years [24, 25]. The enhanced strength-plasticity synergy was achieved in our laminated CrMnFeCoNi/AlCoCrFeNiTi_{0.5} HEA and the corresponding mechanisms were discussed. The promising results of this study pave a road for achieving high-performance HEAs.

Laser engineered net shaping (LENSTM), a typical laser powder-blown AM process, was used in this study. This process is used to produce a 3D part by blowing metal powders into a small-sized melt pool that is created by a focused laser, as schematically shown in Fig. 1 (a). Both constituent powders are perfectly spherical, of a <140 μm diameter (Fig. 1 (b) and (c)). To achieve the laminated structure, these two

powders were loaded into separate powder feeders, and were alternately blown on a layered basis. Bidirectional scans along the Y-axis for the CrMnFeCoNi lamellae and along the X-axis for the AlCoCrFeNiTi_{0.5} lamellae were used (Fig. 1 (d) and (e)), with the following laser processing parameters: laser power 400 W, scan speed 5 mm/s, hatch spacing 460 μm . In order to determine the temperature gradient and cooling rate during the AM process, the melt pool was continuously monitored by a two-wavelength imaging pyrometer that enables high resolution (12.1 $\mu\text{m}/\text{pixel}$) and real-time (25 frames/s) temperature measurements up to 3073 K. After fabrication, laminated HEA specimens were cut out for microstructural investigations with the aid of optical microscopy (OM), scanning electron microscopy (SEM), energy dispersive X-ray spectroscopy (EDS) and electron backscatter diffraction (EBSD). Grinding with emery paper up to 4000 grit size followed by polishing with diamond suspension and colloidal silica-based slurry down to 50 nm was adopted to prepare the examined surface of EBSD specimens. Vickers microhardness (HV) tests at a load of 0.5 kgf and a hold of 15 s were performed to measure the hardness of both constituent lamellae. The compressive tests were performed on the as-deposited laminated HEAs at room temperature and at a strain rate of 10^{-3} s^{-1} , with the load axis normal or parallel to the laminate plane (i.e. XY-plane).

Fig. 2 (a) shows a well-defined laminated structure, with bright CrMnFeCoNi lamellae and dark AlCoCrFeNiTi_{0.5} lamellae. The CrMnFeCoNi/AlCoCrFeNiTi_{0.5} interfaces are clear, but develop some waviness (i.e. melt pool boundary) that is intrinsic to the AM process. The CrMnFeCoNi and AlCoCrFeNiTi_{0.5} lamellae were measured to be 65% and 35%, respectively, based on their area fractions. It should be noted that different area fractions of both HEAs are due to different powder feed rates used in this

study despite the same laser processing parameters (e.g. laser power and laser scan speed). The EBSD inverse pole figure (IPF) map in Fig. 2 (b) reveals the formation of columnar grains in the CrMnFeCoNi lamellae and equiaxed grains in the AlCoCrFeNiTi_{0.5} lamellae, leading to an abrupt grain microstructure transition across the interfaces. Normally, the grain structure of a specific alloy formed during solidification (e.g. laser welding and casting) is controlled by temperature gradient G to solidification velocity V ratio (G/V). To be more specific, a high G/V ratio often promotes the formation of columnar grains, and a low G/V ratio often promotes the formation of equiaxed grains [26]. For example, the weldments' fusion zone is often dominated by columnar microstructures, possibly with equiaxed microstructures at the centerline of the welds where G/V ratio reaches the minimum value [27, 28]. Similarly, the as-cast ingots often comprise a columnar zone in the vicinity of mould walls (high G/V ratio regions) and an equiaxed zone in the center of the moulds (low G/V ratio regions), although a thin chill zone of equiaxed grains and a mixed zone of columnar plus equiaxed grains may be also formed [29-31]. It should be noted, however, that the G values established in the AM process are often extremely large (e.g. 207 K/mm for CrMnFeCoNi lamellae, see Supplementary Fig. 1; versus e.g. 0.1–10 K/mm in casting [29-31]), leading to a substantial G/V ratio and often suppressing the formation of equiaxed grains. That explains why columnar microstructures are more frequently observed for the AM-ed alloys [24, 32-34] and supports the formation of columnar microstructures in the CrMnFeCoNi lamellae.

But surprisingly, we observed a dominantly equiaxed microstructure in the

AlCoCrFeNiTi_{0.5} lamellae. According to the classic solidification theory [35], in directional solidification, solute atoms pile up ahead of the solidification interface, assuming the distribution coefficient less than unity, which will create a solute concentration field $C_i(z)$ and hence an equilibrium solidification temperature field $T_{\text{liquidus}}(z)$. Here the subscript i denotes the component and z denotes the distance from the solidification interface. When the actual temperature $T(z)$ is lower than the equilibrium solidification temperature $T_{\text{liquidus}}(z)$, a constitutionally undercooled region will be established. Within this undercooled region, the equiaxed crystals may nucleate and then grow in the ahead of the growing columnar grains if the nucleation undercooling ΔT_n is reached (i.e. $\Delta T(z) = T_{\text{liquidus}}(z) - T(z) \geq \Delta T_n$). As proposed by Hunt [35], when the volume fraction of equiaxed crystals ϕ reaches a critical value of 49% or above, the columnar growth is prohibited and the columnar grains are replaced by equiaxed grains. Such a columnar-to-equiaxed transition mechanism is schematically shown in Fig. 2 (g). In this paper, the ϕ value of the AlCoCrFeNiTi_{0.5} HEA was estimated with the aid of the Gäumann's model [36], which considers high velocity effects and can be used for rapid solidification. The Gäumann's model estimates the volume fraction of equiaxed crystals ϕ in the undercooled liquid by [36]:

$$\phi = 1 - \exp\left(-\frac{4\pi R_e^3 N_0}{3}\right) \quad (1)$$

with

$$R_e = \int_0^{z_n} \frac{V_e(z)}{V} dz$$

$$V_e(z) = \frac{A \cdot [\Delta T(z)]^2}{\sum_{i=1}^{n-1} C_i(z)}$$

where N_0 is the nucleation site density, R_e is the equiaxed crystal size, $V_e(z)$ is the equiaxed crystal growth velocity, A is the solidification constant, z_n is the distance from the solidification interface to the position where the local undercooling equals the nucleation undercooling, i.e. $\Delta T(z_n) = \Delta T_n$. Similar to original calculations performed by the Gäumann's model, the solidification constant A is taken as $3 \times 10^{-4} \text{ m s}^{-1} \text{ wt.\%/K}^2$ [36]. The nucleation site density N_0 is taken as $3 \times 10^9 / \text{mm}^3$, as estimated in Ref. [37]. Furthermore, $C_i(z)$ and $\Delta T(z)$ profiles can be evaluated by assuming marginal stability of dendrite growth [36, 37]. The above calculations can get a columnar-to-equiaxed transition curve, consisting of a series of solidification conditions that result in $\phi = 49\%$, as shown in Fig. 2 (h). In this study, the solidification condition (as indicated by the red point in Fig. 2 (h)) of the AlCoCrFeNiTi_{0.5} HEA results in a ϕ value greater than 49% and hence locates above the curve, indicating that the columnar growth will be prohibited and replaced by equiaxed growth. This is very consistent with our experimental observation that a few slightly elongated grains are formed at the bottom of the AlCoCrFeNiTi_{0.5} lamellae (i.e. near to the CrMnFeCoNi \rightarrow AlCoCrFeNiTi_{0.5} interfaces), and are soon replaced by equiaxed grains (Fig. 2 (b)). Furthermore, rapid quenching effects of the order of 10^3 K/s (see Supplementary Fig. 1) result in very fine grain microstructures in both constituent alloys. Based on high angle grain boundaries (HAGBs, in black, misorientation $> 15^\circ$) in the IPF map, the average columnar grain width in the CrMnFeCoNi lamellae was determined to be $24 \mu\text{m}$ and the average equiaxed grain diameter in the AlCoCrFeNiTi_{0.5} lamellae was determined to be $7 \mu\text{m}$.

Furthermore, both constituent alloys show very random crystallographic textures, as evidenced by the random grain colors in the IPF map.

Fig. 2 (c) gives the EBSD phase map of the FCC CrMnFeCoNi lamellae and BCC AlCoCrFeNiTi_{0.5} lamellae. It should be noted that besides the major BCC phases, a small amount of discrete FCC phases at the grain boundaries was also observed in the AlCoCrFeNiTi_{0.5} lamellae. This can be more clearly observed in the back-scattered electron (BSE) image in Fig. 2 (f). The AlCoCrFeNiTi_{0.5} HEA was reported to be free of FCC phases [5, 37]. Concerning this point, the formation of FCC phases in the AlCoCrFeNiTi_{0.5} lamellae is ascribed to the introduction of a small amount of CrMnFeCoNi constituents (see Supplementary Fig. 2), through partial remelting of the previous layer followed by simultaneous solidification. Moreover, very good metallurgical bonding is achieved at the CrMnFeCoNi/AlCoCrFeNiTi_{0.5} interfaces (Fig. 2 (d), (e) and (f)), and no obvious defects (e.g. oxide particles, frequently observed in diffusion-bonded laminates [38, 39]) are formed. Finally, the remarkable differences in the phases and microstructures across the CrMnFeCoNi/AlCoCrFeNiTi_{0.5} interfaces lead to a distinct difference in microhardness, with 197 HV in the CrMnFeCoNi lamellae and 657 HV in the AlCoCrFeNiTi_{0.5} lamellae.

Typical compressive stress-strain curves corresponding to both loading cases of the CrMnFeCoNi/AlCoCrFeNiTi_{0.5} laminated HEA are plotted in Fig. 3. It is noted that this laminated HEA exhibits a remarkable combination of yield strength and macroscopic plasticity, surpassing those of reported high-strength bulk refractory HEAs, e.g. NbMoTaW [4], VNbMoTaW [4], TaNbHfZrTi [40] and NbCrMo_{0.5}Ta_{0.5}TiZr [41]. The

compressive yield strengths of these monolithic refractory HEAs are normally above 1000 MPa, but they fail in a much more brittle manner with compressive plasticity of below e.g. 30 ~ 40% or even a few percent. The yield strengths of this laminated HEA are anisotropic, and were determined to be ~ 888 and 990 MPa, respectively, for normal and parallel loading cases. For the parallel loading case (i.e. an iso-strain case), the strong AlCoCrFeNiTi_{0.5} lamellae carry the load, and the soft CrMnFeCoNi lamellae only transfer the load to the AlCoCrFeNiTi_{0.5} lamellae, resulting in a harder orientation and hence a higher yield strength [13, 42, 43]. The yield strength of the laminated alloys has been previously reported to scale with the volume fractions and yield strengths of constituent alloys, i.e. rule of mixture [44]. Hence, the compressive properties of the LENSTM-deposited and as-casted monolithic HEAs are also tested, and shown in Fig. 3. No obvious anisotropic compressive properties were found for these two constituent alloys, and this may be attributed to the random crystallographic textures developed in both alloys. Assuming the rule of mixture, where $\sigma_{ys} = f_1 \cdot \sigma_{ys,1} + f_2 \cdot \sigma_{ys,2}$ (f_i represents the volume fraction of constituent i ; $\sigma_{ys,i}$ represents the yield strength of constituent i), the yield strength of this laminated HEA is calculated to be 847 MPa. This value constitutes a substantial portion of the measured yield strength, especially for the normal loading case, suggesting that the high yield strength of this laminated HEA primarily originates from the high-strength AlCoCrFeNiTi_{0.5} lamellae that are BCC structured and fine equiaxed-grained.

Furthermore, we note that this laminated HEA shows a substantial and steady work hardening mechanism and hence good macroscopic plasticity, without premature

complete fracture. To understand the origin of the resistance to complete failure of this laminated HEA, multi-cycle loading-unloading compressive tests were performed, and after each cycle, the specimen was ex-situ examined by SEM (Fig. 4). When the load axis is normal to the laminate plane, damage evolves by transverse cracking (i.e. normal to the interfaces) in the AlCoCrFeNiTi_{0.5} lamellae and terminating at the interfaces (Fig. 4 (a1)), with a few discrete transverse cracks (Fig. 4 (a2)). With straining, more transverse cracks are formed within the AlCoCrFeNiTi_{0.5} lamellae, and the earlier cracks broaden (Fig. 4 (b1)). Note that these cracks do not connect and are bridged by the ductile CrMnFeCoNi lamellae. Furthermore, it is noted that the tips of the cracks generate shear bands in the adjacent CrMnFeCoNi lamellae (Fig. 4 (b2)). This indicates that strain localization, rather than homogenous deformation, has occurred in the CrMnFeCoNi lamellae. The local plastic deformation in the CrMnFeCoNi lamellae is quite reasonable since the crack tip can create a strong stress field [45]. It has been reported elsewhere that the plastic deformation at the crack tip in FCC alloys can be accommodated by various contributors (e.g. lattice dislocation emission [45], stacking fault formation [46], mechanical twinning [46, 47] and strain-induced martensitic transformation [48, 49]), and can in turn blunt the crack tip and hence suppress the crack growth. It is already relatively clear and well documented that dislocation motion plus mechanical twinning dominate the plastic deformation behavior of the FCC CrMnFeCoNi HEA, and no clear phase transformation can be detected [9, 50]. Therefore, in this study the crack blunting has been attributed to dislocation motion and mechanical twinning induced from the crack tip. With further straining, the shear bands

initiated by two separate cracks may connect (Fig. 4 (c1) and (c2)), and finally shear cracks are formed in the ductile CrMnFeCoNi lamellae (Fig. 4 (d1) and (d2)). For such a loading case (i.e. an iso-stress case), the rigid AlCoCrFeNiTi_{0.5} lamellae delay the occurrence of macro-plastic deformation and hence delay the yielding of the complete specimen. During straining, the soft CrMnFeCoNi lamellae in turn bridge the cracked AlCoCrFeNiTi_{0.5} lamellae and hence avoid premature complete failure of the specimen. When the load axis is parallel to the laminate plane, damage evolves by longitudinal (i.e. parallel to the interfaces) cracking within the brittle AlCoCrFeNiTi_{0.5} lamellae (Fig. 4 (e1) and (f1)). Such longitudinal cracks are believed to nucleate from both ends which directly contact the crossheads (as indicated in Fig 4 (e1)). The larger cracks may branch into several smaller cracks which finally terminate at the interfaces (Fig. 4 (e2) and (f2)). With straining, frequent crushing was observed in the AlCoCrFeNiTi_{0.5} lamellae (Fig. 4 (g2) and (h2)). Furthermore, it is interesting to note that the right side AlCoCrFeNiTi_{0.5} lamella seems to buckle together with adjacent CrMnFeCoNi lamellae, and the CrMnFeCoNi/AlCoCrFeNiTi_{0.5} interfaces are surprisingly intact during straining (Fig. 4 (g1) and (h1)). This is beyond expectation, and as reported in Refs [13, 17], it is more common that delamination occurs along the interfaces and then the ductile lamellae bend independently. Overall speaking, for both loading orientations, the soft CrMnFeCoNi lamellae desirably bridge the cracked AlCoCrFeNiTi_{0.5} lamellae, and the good interfacial metallurgical bonding effectively prevents the interfacial failure, both of which prevent premature complete failure of this laminated HEA.

To sum up, we additively manufactured a CrMnFeCoNi/AlCoCrFeNiTi_{0.5}

laminated HEA that exhibits an enhanced synergy of yield strength and macroscopic plasticity during compression, surpassing those of monolithic bulk HEAs. The high strength is attributed to the ultra-hard BCC equiaxed grains in the AlCoCrFeNiTi_{0.5} lamellae. The large macroscopic plasticity is ascribed to the fact that the soft CrMnFeCoNi lamellae bridge the cracked AlCoCrFeNiTi_{0.5} lamellae, and the good interfacial metallurgical bonding prevents the interfacial failure. This study demonstrates that multi-phase laminated HEAs with superior compressive properties can be successfully synthesized by the laser powder-blown AM process, and we expect that such AM-ed multi-phase laminated HEAs can also lead to similar improvements in tensile properties etc., despite possible tension-compression asymmetry in both yielding and strain hardening behaviors.

Acknowledgement

This work was supported by the Research Committee of The Hong Kong Polytechnic University through research student project (account code: G_RUHS).

References

- [1] J.W. Yeh, S.K. Chen, S.J. Lin, J.Y. Gan, T.S. Chin, T.T. Shun, C.H. Tsau, S.Y. Chang, *Adv. Eng. Mater.* 6 (2004) 299-303.
- [2] B. Gludovatz, A. Hohenwarter, D. Catoor, E.H. Chang, E.P. George, R.O. Ritchie, *Science* 345 (2014) 1153-1158.
- [3] W.H. Liu, Y. Wu, J.Y. He, T.G. Nieh, Z.P. Lu, *Scr. Mater.* 68 (2013) 526-529.
- [4] O.N. Senkov, G.B. Wilks, J.M. Scott, D.B. Miracle, *Intermetallics* 19 (2011) 698-

706.

- [5] Y.J. Zhou, Y. Zhang, T.N. Kim, G.L. Chen, *Mater. Lett.* 62 (2008) 2673-2676.
- [6] Y. Yu, J. Wang, J. Li, H. Kou, W. Liu, *Mater. Lett.* 138 (2015) 78-80.
- [7] X.Z. Gao, Y.P. Lu, B. Zhang, N.N. Liang, G.Z. Wu, G. Sha, J.Z. Liu, Y.H. Zhao, *Acta Mater.* 141 (2017) 59-66.
- [8] P.J. Shi, W.L. Ren, T.X. Zheng, Z.M. Ren, X.L. Hou, J.C. Peng, P.F. Hu, Y.F. Gao, Y.B. Zhong, P.K. Liaw, *Nat. Commun.* 10 (2019).
- [9] G. Laplanche, A. Kostka, O.M. Horst, G. Eggeler, E.P. George, *Acta Mater.* 118 (2016) 152-163.
- [10] D. Embury, O. Bouaziz, *Annu. Rev. Mater. Res.* 40 (2010) 213-241.
- [11] R. Cicoria, B. Chehab, H. Zurob, *Scr. Mater.* 68 (2013) 17-21.
- [12] B. Chéhab, H. Zurob, D. Embury, O. Bouaziz, Y. Brechet, *Adv. Eng. Mater.* 11 (2009) 992-999.
- [13] A. Rohatgi, D.J. Harach, K.S. Vecchio, K.P. Harvey, *Acta Mater.* 51 (2003) 2933-2957.
- [14] Y. Li, Q. Zhou, S. Zhang, P. Huang, K. Xu, F. Wang, T. Lu, *Appl. Surf. Sci.* 433 (2018) 957-962.
- [15] D.O. Cox, A.S. Tetelman, *J. Adhes.* 5 (1973) 279-300.
- [16] H. Wu, G.H. Fan, B.C. Jin, L. Geng, X.P. Cui, M. Huang, *Mater. Des.* 89 (2016) 697-702.
- [17] T. Li, F.C. Jiang, E.A. Olevsky, K.S. Vecchio, M.A. Meyers, *Mater. Sci. Eng. A* 443 (2007) 1-15.

- [18] A.B. Pandey, B.S. Majumbar, D.B. Miracle, *Acta Mater.* 49 (2001) 405-417.
- [19] F. Kummel, T. Hausol, H.W. Hoppel, M. Goken, *Acta Mater.* 120 (2016) 150-158.
- [20] X.L. Ma, C.X. Huang, J. Moering, M. Ruppert, H.W. Hoppel, M. Goken, J. Narayan, Y.T. Zhu, *Acta Mater.* 116 (2016) 43-52.
- [21] Y. Du, G.H. Fan, T.B. Yu, N. Hansen, L. Geng, X.X. Huang, *Mater. Sci. Eng. A* 673 (2016) 572-580.
- [22] M.Y. Seok, J.A. Lee, D.H. Lee, U. Ramamurty, S. Nambu, T. Koseki, J.I. Jang, *Acta Mater.* 121 (2016) 164-172.
- [23] Y.M. Wang, T. Voisin, J.T. McKeown, J.C. Ye, N.P. Calta, Z. Li, Z. Zeng, Y. Zhang, W. Chen, T.T. Roehling, R.T. Ott, M.K. Santala, P.J. Depond, M.J. Matthews, A.V. Hamza, T. Zhu, *Nat. Mater.* 17 (2018) 63.
- [24] Z.G. Zhu, Q.B. Nguyen, F.L. Ng, X.H. An, X.Z. Liao, P.K. Liaw, S.M.L. Nai, J. Wei, *Scr. Mater.* 154 (2018) 20-24.
- [25] Y. Brif, M. Thomas, I. Todd, *Scr. Mater.* 99 (2015) 93-96.
- [26] W. Kurz, C. Bezencon, M. Gäumann, *Sci. Technol. Adv. Mat.* 2 (2001) 185-191.
- [27] G.J. Davies, J.G. Garland, *Int. Met. Rev.* 20 (1975) 83-108.
- [28] J.C. Villafuerte, E. Pardo, H.W. Kerr, *Metall. Trans. A* 21 (1990) 2009.
- [29] J. Lapin, A. Klimova, Z. Gabalcová, *Kovove Mater.* 51 (2013) 147-154.
- [30] J. Lapin, Z. Gabalcová, *Intermetallics* 19 (2011) 797-804.
- [31] A.E. Ares, C.E. Schvezov, *Metall. Mater. Trans. A* 38 (2007) 1485-1499.
- [32] G.P. Dinda, A.K. Dasgupta, J. Mazumder, *Scr. Mater.* 67 (2012) 503-506.
- [33] T. Ishimoto, K. Hagihara, K. Hisamoto, S.H. Sun, T. Nakano, *Scr. Mater.* 132 (2017)

34-38.

[34] S. Guan, D. Wan, K. Solberg, F. Berto, T. Welo, T.M. Yue, K.C. Chan, *Mater. Sci. Eng. A* 761 (2019) 138056.

[35] J.D. Hunt, *Mater. Sci. Engng.* 65 (1984) 75-83.

[36] M. Gäumann, R. Trivedi, W. Kurz, *Mater. Sci. Eng. A* 226 (1997) 763-769.

[37] S. Guan, K. Solberg, D. Wan, F. Berto, T. Welo, T.M. Yue, K.C. Chan, *Mater. Des.* 184 (2019) 108202.

[38] C.M. Cepeda-Jiménez, F. Carreño, O.A. Ruano, A.A. Sarkeeva, A.A. Kruglov, R.Y. Lutfullin, *Mater. Sci. Eng. A* 563 (2013) 28-35.

[39] K. Burger, M. Rühle, *Ultramicroscopy* 29 (1989) 88-97.

[40] O.N. Senkov, J.M. Scott, S.V. Senkova, D.B. Miracle, C.F. Woodward, *J. Alloys Compd.* 509 (2011) 6043-6048.

[41] O.N. Senkov, C.F. Woodward, *Mater. Sci. Eng. A* 529 (2011) 311-320.

[42] S.W. Feng, Q. Guo, Z. Li, G.L. Fan, Z.Q. Li, D.B. Xiong, Y.S. Su, Z.Q. Tan, J. Zhang, D. Zhang, *Acta Mater.* 125 (2017) 98-108.

[43] S. Roy, B. Butz, A. Wanner, *Acta Mater.* 58 (2010) 2300-2312.

[44] X.L. Ma, C.X. Huang, W.Z. Xu, H. Zhou, X.L. Wu, Y.T. Zhu, *Scr. Mater.* 103 (2015) 57-60.

[45] I.A. Ovid'ko, A.G. Sheinerman, *Scr. Mater.* 60 (2009) 627-630.

[46] Y. Zhou, W. Yang, M. Hu, Z. Yang, *Comp. Mater. Sci.* 112 (2016) 27-33.

[47] L. Liu, J. Wang, S.K. Gong, S.X. Mao, *Sci. Rep.* 4 (2014) 4397.

[48] H. Li, M. Koyama, T. Sawaguchi, K. Tsuzaki, H. Noguchi, *Philos. Mag. Lett.* 95

(2015).

[49] Y.-B. Ju, M. Koyama, T. Sawaguchi, K. Tsuzaki, H. Noguchi, *Acta Mater.* 112

(2016) 326-336.

[50] M.J. Jang, S.H. Joo, C.W. Tsai, J.W. Yeh, H.S. Kim, *Met. Mater. Int.* 22 (2016)

982-986.

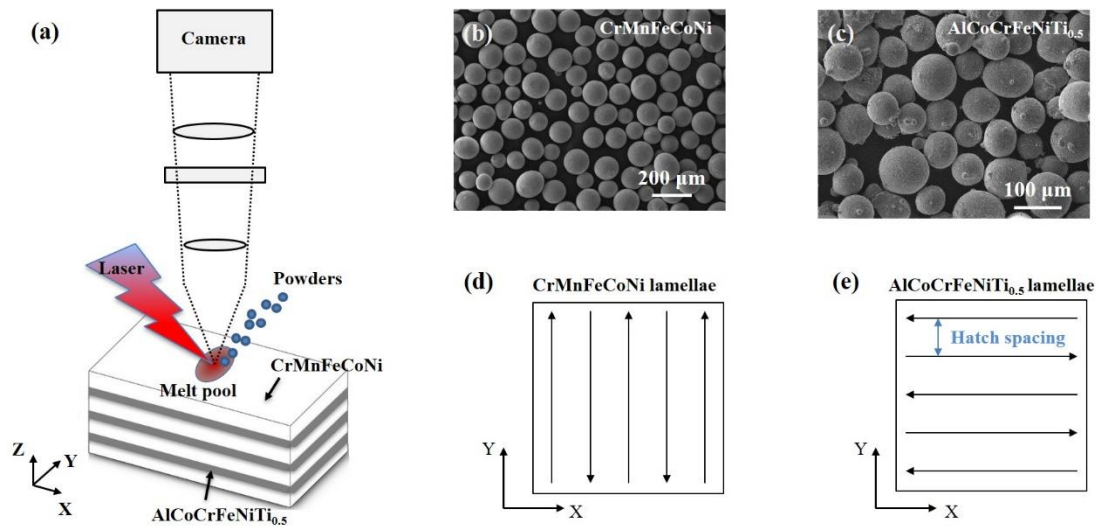


Fig. 1. Synthesis of CrMnFeCoNi/AlCoCrFeNiTi_{0.5} laminated HEA via the LENS™ process. (a) Schematic of the lamination process via the LENS™ technique. (b) CrMnFeCoNi and (c) AlCoCrFeNiTi_{0.5} prealloyed powders. Bidirectional scans (d) along the Y-axis for the CrMnFeCoNi lamellae and (e) along the X-axis for the AlCoCrFeNiTi_{0.5} lamellae.

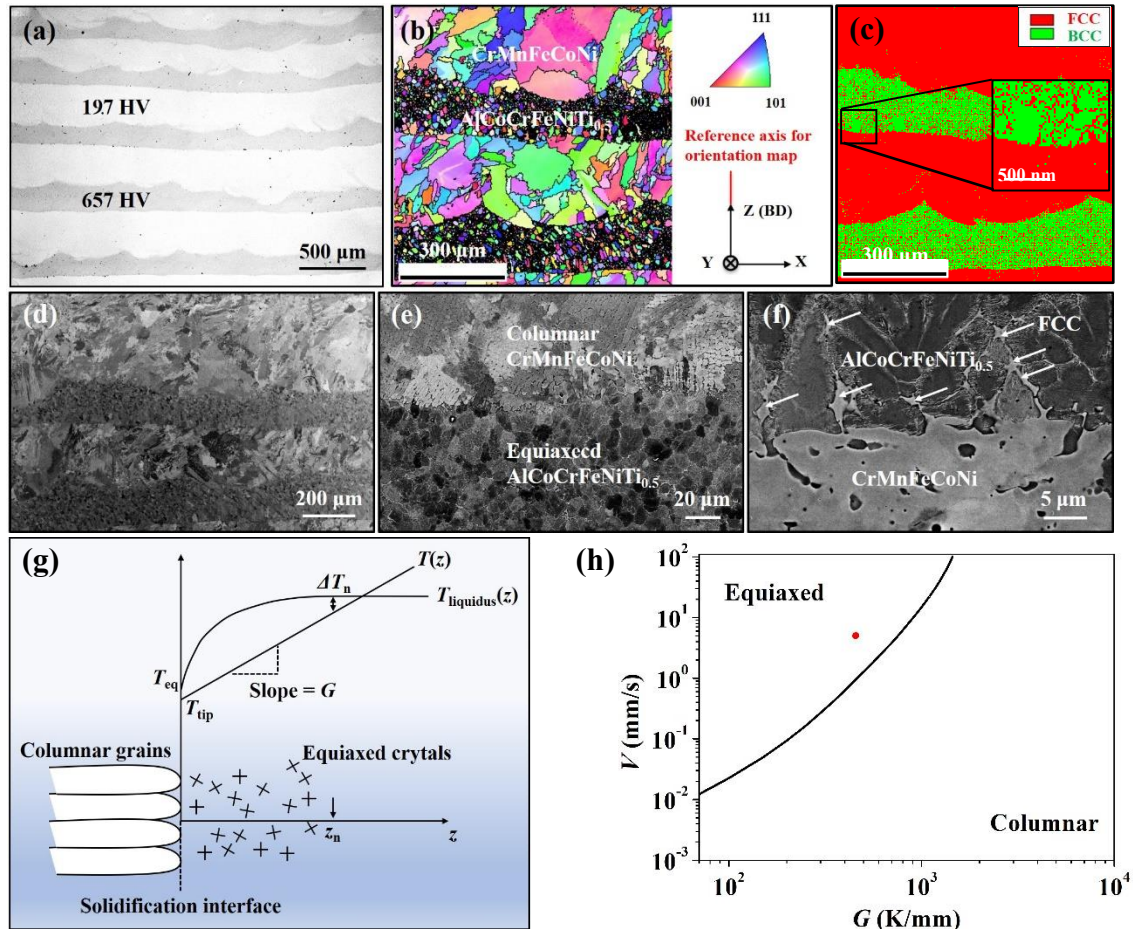


Fig. 2. Microstructures of the LENSTM-deposited CrMnFeCoNi/AlCoCrFeNiTi_{0.5} laminated HEA observed on a XZ cross-section. (a) OM micrograph of a well-defined laminated structure. (b) EBSD IPF map of alternating columnar and equiaxed grain microstructures. The reference axis is the build direction (BD), i.e. Z-axis. (c) EBSD phase map of FCC and BCC phases. (d), (e) and (f) BSE micrographs indicating well-bonded CrMnFeCoNi/AlCoCrFeNiTi_{0.5} interfaces. The arrows in (f) indicate some discrete FCC phases at the substantial BCC's grain boundaries. (g) Schematic view of the columnar-to-equiaxed transition mechanism. Detailed discussion in text. (h) Columnar-to-equiaxed transition curve calculated for the AlCoCrFeNiTi_{0.5} HEA, with the established G - V combination marked by a red point, showing that the formation of

equiaxed microstructures is promoted. The V value is taken as the laser scan speed 5 mm/s.

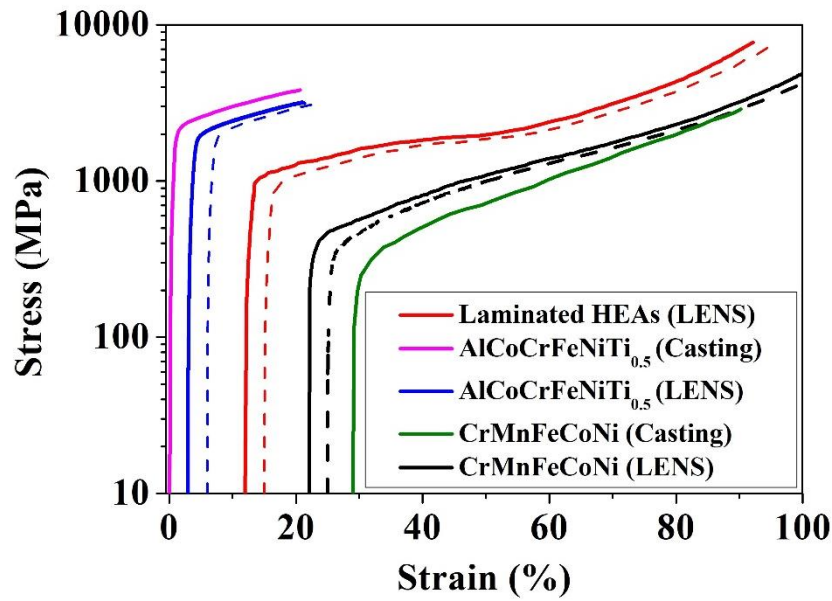


Fig. 3. Typical compressive stress-strain curves of the LENSTM-deposited CrMnFeCoNi/AlCoCrFeNiTi_{0.5} laminated HEA, compared to those of LENSTM-deposited and as-casted monolithic HEAs. For the LENSTM-deposited specimens, compressive tests with the load axis both parallel (solid curves) and normal (dashed curves) to the XY-plane were performed. The compressive tests of the CrMnFeCoNi/AlCoCrFeNiTi_{0.5} laminated HEA and the monolithic CrMnFeCoNi HEA were interrupted. For a better comparison, the compressive stress-strain curves are somewhat shifted towards the right.

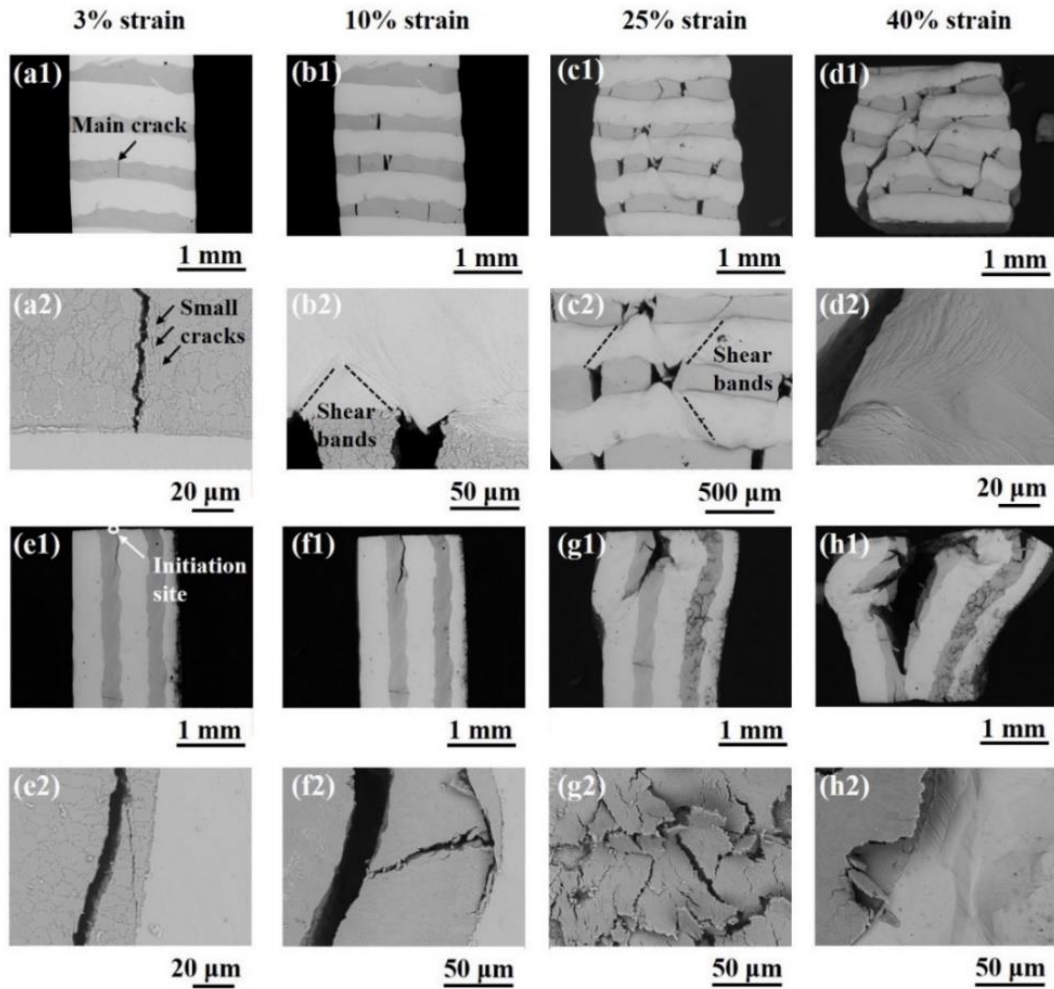


Fig. 4. SEM micrographs showing the progressive damage evolution of the CrMnFeCoNi/AlCoCrFeNiTi_{0.5} laminated HEA during compression, with the load axis normal (a1 – d2) or parallel (e1 – h2) to the laminate plane. The corresponding strain values are indicated at the top. (a2 – d2) and (e2 – h2) are a magnified view of the characteristics in (a1 – d1) and (e1 – h1), respectively.